Journal of the Chinese Society of Mechanical Engineers, Vol.46, No.6, pp619~631 (2025)

Path Synthesis of Spherical Four-Bar Linkages Using Spatial Elliptical Fourier Descriptors

Yuan Chang*, Jia-Ling Chang** and Jyh-Jone Lee***

Keywords： **Spherical four-bar linkages, Path synthesis, Elliptical Fourier descriptor, Open curve**

ABSTRACT

Numerous researchers have employed various shape descriptors in the dimensional synthesis of mechanisms. This study introduces a methodology for the path synthesis of spherical four-bar linkages utilizing Elliptical Fourier Descriptors (EFDs). EFDs, a Fourier-based shape representation method, allow the independent acquisition of Fourier coefficients through the Fourier expansion of individual components of the 3D coupler curve, rather than relying on a function as in traditional Fourier analysis. This approach eliminates the need to project the curve onto any plane for Fourier analysis, while preserving invariance characteristics under similarity transformations. Additionally, a method for establishing the shape signature for the open curve is developed. By integrating this process with traditional EFD and optimization algorithm, the proposed method becomes essentially applicable for synthesizing spatial four-bar linkages for both open and closed curves in a single-step design process. Finally, the effectiveness of the proposed method is demonstrated through several examples of spherical four-bar linkages.

INTRODUCTION

Spherical four-bar linkages exhibit diverse applications, serving not only as mechanical components like the Hooke joint but also functioning as integral subsystems within various machinery, such as automobiles, robots (Chablat and Angeles, 2003, Wang et al., 2022), and medical instruments (Lum et al., 2006, Arata et al., 2018). Therefore, a significant focus in design lies in the dimensional synthesis of spherical four-bar mechanisms, which primarily determines the dimensions of linkages that can be designed to produce specific types of motion. Over the past decades, various methods have been developed for the dimensional synthesis of spherical four-bar linkages. These approaches encompass geometric methods (Bagci, 1984), numerical techniques covering both limited and unlimited positions (Lin, 1998, Suixian et al., 2009, Lee et al., 2009), shape representation methods (McGarva and Mullineux, 1993, McGarva, 1994, Ullah and Kota, 1997, Wu et al., 2011, Sun and Chu, 2010, Chu and Sun, 2010, Mullineux, 2011, Galán-Marín et al. 2009, Sun et al., 2015, Sun et al., 2018), and/or combinations thereof. A workflow of applying shape representation method upon path generation usually contains numerical atlas of the shape descriptors and/or the optimization algorithm that searches best shape descriptors of the target. Among the various shape representation methods, Fourier descriptor (FD) is notable as one of the most widely utilized techniques, involving the decomposition of a contour into frequency components through Fourier series analysis. While the use of FD is effective for planar curves, applying it to spatial curves poses a significant challenge, often requiring the adoption of ad hoc approaches. Sun and Chu (2010) introduced a three-dimensional (3D) Fourier series to characterize the coupler curves of spatial linkages. They projected the 3D data onto a two-dimensional *y*-*z* plane and a one-dimensional *x*-axis for Fourier analysis, while also establishing complex geometric conditions in the process. Further, they applied this approach to the path synthesis of the spherical mechanism (Chu and Sun, 2010). However, the method did not eliminate the influence of the rotations about the *y*- and *x*-axes. Mullineux (2011) proposed an alternative approach to Fourier analysis for the curve on a sphere using gnomonic projection. This method involves choosing a point on the surface of the sphere and projecting the sphere onto the plane tangent to this point. Since the gnomonic projection originates from the center of the sphere, it can represent less than half of the sphere's surface area. Further, the distortion of the mapping increases from the center (tangent point) to the periphery. Figure 1

Paper Received December, 2024. Revised March, 2025. Accepted April, 2025. Author for Correspondence: Jyh-Jone Lee.

* *Graduate Student, Department of Mechanical Engineering, National Taiwan University, Taipei, Taiwan 106.*

** *Graduate Student, Department of Mechanical Engineering, National Taiwan University, Taipei, Taiwan 106.*

*** *Professor, Department of Mechanical Engineering, National Taiwan University, Taipei, Taiwan 106. Email:jjlee@ntu.edu.tw*

illustrates a scenario in which the curve generated by a spherical four-bar linkage spans more than a hemisphere. Such a curve cannot be represented by the gnomonic projection, as it extends beyond a hemisphere. Additionally, it can be observed in Fig. 1(b) that when the curve is distant from the *z*-axis (central axis), the projected profile more closely resembles a circular curve rather than a general closed curve. These are the shortcomings of using the projection method.

Nonetheless, among various works that have utilized Fourier shape analysis, one noteworthy approach is the use of elliptical Fourier descriptors (EFDs) as proposed by Kuhl and Giardina (1982). EFD is also based on Fourier analysis. It independently decomposes the cumulative chordal length of the *x* and *y* components of the outline into harmonically related trigonometric series, comprising sine and cosine functions. For any given harmonic, it geometrically depicts an ellipse. Thus, the position of any point on the outline can be approximated by the net displacement of a point traversing a series of superimposed and successively smaller ellipses. EFDs have been applied in various fields such as patter recognition (Lin and Hwang, 1987), biology (Lestrel, 1997, Godefroy et al., 2012, Crampton, 1995), anthropology (Caple et al., 2017), and dentistry (Niño-Sandoval et al., 2018). In summarizing the works presented in Chapter 2 of Godefroy et al. (2012) and Crampton (1995), EFD method has shown notable features compared to the traditional Fourier descriptors in the following aspects:

1. Parameterization sensitivity: Traditional Fourier descriptors are more sensitive to the choice of starting point and parameterization method than EFDs. The requirement of equal intervals along the outline is relaxed by using EFD, which allows for closer spacing on high-curvature portions of the curve.
2. Handling of complex shapes: EFDs perform better with certain complex shapes, while traditional Fourier descriptors may encounter difficulties. This was demonstrated by the work shown in Fig. 5 of Lestrel and Roche1 (1986) where EFDs effectively handled complex shapes with multi-valued radii and curves that bend back, as well as the work shown in Fig. 1 of Chang et al. (2024) where the curve has a cusp.
3. Normalization complexity and geometric intuition: Rotation, translation, and scale invariance can be achieved more systematically with EFDs than with traditional Fourier descriptors, particularly for a 3D curve (discussed in a later section). In addition, the coefficients of EFD are normalized and associated with intuitive geometric interpretations through ellipses, making it easier to visualize and understand the shape's features.
4. Easy extension to three dimension: The extension of EFD to 3D outlines requires only a straightforward approach by incorporating an additional equation for the third dimension.

In light of the advantages mentioned and the notable absence of their application in the path synthesis of spatial mechanisms, this paper presents a systematic approach to shape description for three-dimensional curves using EFDs. Furthermore, we expand its applicability from closed to open curves. Leveraging the superior capabilities of EFDs in approximating complex curves with high curvature, we propose a novel process for the representation of non-periodic trajectories utilizing the EFD-based technique. This approach involves tracing the open curve, curving back at the end, and then retracing the path to the initial point, thereby creating a closed curve configuration. The converted curve is then used as the shape signature of the original open curve. While enhancing the accuracy of depicting the converted curve by potentially increasing the number of harmonics in this approach, the computational efficiency and effectiveness can be maintained due to the algebraic computing scheme employed for the EFD coefficients. Additionally, the similarity transformation remains applicable. Subsequently, an optimization algorithm using the Differential Evolution (DE) algorithm is introduced to optimize the linkage parameters by comparing the Fourier coefficients. As a result, this process establishes a comprehensive method for path synthesis of spherical four-bar linkages for both closed and open curves, via EFD within a unified scheme.

The organization of the paper is as follows. The second section provides the mathematical background of EFD and its specific treatment of open curves. The third section elaborates on the process of normalizing the 3D curves under consideration. The fourth section discusses the linkage parameters of a spherical four-bar linkage essential for design purposes, along with the algorithms employed to obtain the optimal linkage configuration. The fifth section presents numerical examples to illustrate the effectiveness of the proposed methodology. The final section concludes the article.

SPATIAL ELLIPTICAL FOURIER DESCRIPTORS

Approximation for a Closed Curve

In conventional Fourier analysis, a closed curve is typically represented using a parametric function, and the function is then expanded into a Fourier series for further analysis. The EFA performs the analysis in a comparable manner with the key difference being that it deals with the components of a closed curve individually. Each of these components, comprising of the sine and cosine functions, depicts an ellipse within the domain where the curve exists. As EFA treats the individual components of a curve rather than the entire function, it can be readily extended to the three-dimensional scenario. Consider a point P on a given three-dimensional curve, and denote its coordinates as

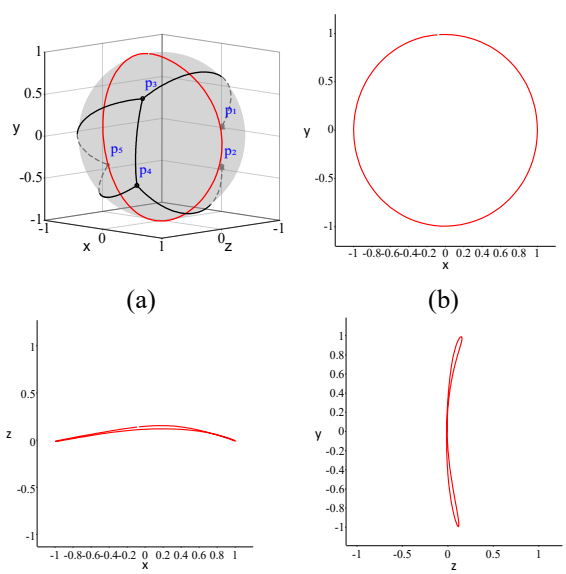

Fig. 1. (a) Coupler curve generated by a spherical four-bar linkage. p_1, p_2, p_3 and p_4 are the positions of revolute joints while p_5 is the coupler point that traces a coupler curve drawn by red line. (b) Curve projected onto *y*-*x* plane (c) Curve projected onto *z*-*x* plane (d) Curve projected onto *y*-*z* plane

$[x(t), y(t), z(t)]$ where t is the parameter defining the curve over a 2π period. Taking the Fourier expansion of each component and writing it in matrix form, one can obtain:

$$\begin{bmatrix} x(t) \\ y(t) \\ z(t) \end{bmatrix} = \begin{bmatrix} A_0 \\ C_0 \\ E_0 \end{bmatrix} + \sum_{n=1}^{N} \begin{bmatrix} a_n & b_n \\ c_n & d_n \\ e_n & f_n \end{bmatrix} \begin{bmatrix} \cos nt \\ \sin nt \end{bmatrix} \quad (1)$$

where n is the harmonic number, N is the maximum harmonic number, $(a_n,\ b_n,\ c_n,\ d_n,\ e_n,\ f_n)$ are the coefficients of the n^{th} harmonic, and $(A_0,\ C_0,\ E_0)$ are the term that defines the shape centroid. The coefficients of the n^{th} harmonic can be calculated from integrals of the product of the component and cosine/sine over the time period as in the continuous Fourier series. Nonetheless, Kuhl and Giardina (1982) took an algebraic approach to these coefficients by discretizing the curve into small segments, resulting in an efficient computation of the coefficients. A detailed derivation for planar case can be found in Kuhl and Giardina (1982). The coefficients of the n^{th} harmonic for three-dimensional case can be derived in a manner similar to that of the 2D case as:

$$a_n = \frac{1}{n^2\pi}\sum_{p=1}^{K-1}\frac{\Delta x_p}{\Delta L_p}\left(\cos nt_{p+1} - \cos nt_p\right) \quad (2.a)$$

$$b_n = \frac{1}{n^2\pi}\sum_{p=1}^{K-1}\frac{\Delta x_p}{\Delta L_p}\left(\sin nt_{p+1} - \sin nt_p\right) \quad (2.b)$$

$$c_n = \frac{1}{n^2\pi}\sum_{p=1}^{K-1}\frac{\Delta y_p}{\Delta L_p}\left(\cos nt_{p+1} - \cos nt_p\right) \quad (2.c)$$

$$d_n = \frac{1}{n^2\pi}\sum_{p=1}^{K-1}\frac{\Delta y_p}{\Delta L_p}\left(\sin nt_{p+1} - \sin nt_p\right) \quad (2.d)$$

$$e_n = \frac{1}{n^2\pi}\sum_{p=1}^{K-1}\frac{\Delta z_p}{\Delta L_p}\left(\cos nt_{p+1} - \cos nt_p\right) \quad (2.e)$$

$$f_n = \frac{1}{n^2\pi}\sum_{p=1}^{K-1}\frac{\Delta z_p}{\Delta L_p}\left(\sin nt_{p+1} - \sin nt_p\right) \quad (2.f)$$

where p is the point number; K is the total number of points on the curve; $\Delta x_p = x_{p+1} - x_p$, $\Delta y_p (= y_{p+1} - y_p)$, and $\Delta z_p (= z_{p+1} - z_p)$ are the distance between two consecutive points along the *x*, *y*, and *z*-axes, respectively; $\Delta L_p = \sqrt{(\Delta x_p)^2 + (\Delta y_p)^2 + (\Delta z_p)^2}$ is the Euclidean distance between two points. In addition, the time elapsed is calculated as the current cumulative length divided by the total length:

$$t_p = \frac{2\pi\sum_{i=1}^{p}\Delta L_i}{\sum_{p=1}^{K}\Delta L_p} \quad (3)$$

Furthermore, the constant terms $(A_0,\ C_0,\ E_0)$ are actually equivalent to the zero harmonic coefficients (a_0, c_0, e_0), while (B_0, D_0, F_0) are equal to zero. The constant terms are calculated as:

$$A_0 = \sum_{p=1}^{K}\frac{\Delta x_p}{2\Delta L_p}\left(t_p^2 - t_{p-1}^2\right) + \left(\sum_{i=1}^{p-1}\Delta x_i - \frac{\Delta x_p}{\Delta L_p}\sum_{i=1}^{p-1}\Delta t_j\right)\left(t_p - t_{p-1}\right) \quad (4.a)$$

$$C_0 = \sum_{p=1}^{K}\frac{\Delta y_p}{2\Delta L_p}\left(t_p^2 - t_{p-1}^2\right) + \left(\sum_{i=1}^{p-1}\Delta y_i - \frac{\Delta y_p}{\Delta L_p}\sum_{i=1}^{p-1}\Delta t_j\right)\left(t_p - t_{p-1}\right) \quad (4.b)$$

$$E_0 = \sum_{p=1}^{K}\frac{\Delta z_p}{2\Delta L_p}\left(t_p^2 - t_{p-1}^2\right) + \left(\sum_{i=1}^{p-1}\Delta z_i - \frac{\Delta z_p}{\Delta L_p}\sum_{i=1}^{p-1}\Delta t_j\right)\left(t_p - t_{p-1}\right) \quad (4.c)$$

Fig. 2(a) illustrates the geometric meaning of the spatial EFDs. A curve in 3D is approximated by a series of spatial ellipses that superimpose upon one another, ranging from large to small. Each ellipse is constructed by the corresponding harmonic. Fig. 2(b) depicts the first ellipse in which $\boldsymbol{u}_1$ and $\boldsymbol{v}_1$ are the semi-major and semi-minor axes, respectively. Angle θ_1 is the phase angle between the starting point (t=0) and the semi-major axis. This phase angle concerns about the phase shift if one wishes to shift the starting point from one point to another new point. On the other hand, the orientation of the first ellipse is now presented in three dimension with respect to the fixed frame. Therefore, a relationship between the Fourier coefficients and the orientation of the first ellipse must be established. The relations among the Fourier coefficients, phase shift, and orientations of the ellipses are essential to the normalization process and will be discussed in Section 2.3.

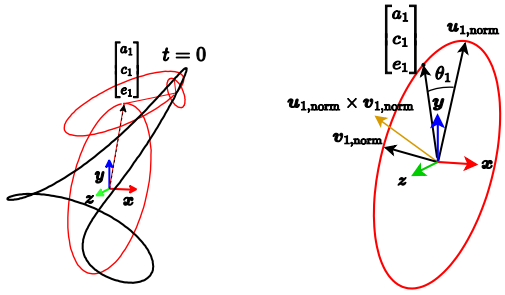

(a) (b)

Fig. 2. Geometric meaning of the spatial EFDs (a) contour described by a series of ellipses (b) the first ellipse and phase shift θ_1.

Approximation for an Open Curve

The traditional FD and EFD can only be applied to closed curves, that is, periodic functions. Wu *et al.* (2011) used the trigonometric polynomial curve fitting (TPCF) technique to approximate open curves, where the *x* and *y* components of a point are represented by a finite series of sine and cosine functions. The TPCF for acquiring coefficients has been demonstrated to be less efficient compared to the original EFD by Chang et al. (2024), as it requires least-square curve fitting computation and involves two-step optimization searching. Moreover, the TPCF is applicable to the planar case. In this study, we introduce a novel method to establish a shape signature wherein Fourier coefficients can then be utilized to represent an open curve. As shown in Fig. 3, an open curve with *K* points is converted to a closed curve by first tracing it from one end to the other end and then retracing the same path back to the starting point. The point *P* on the forward path is made coincident with the point (2*K*-*P*) on the backward path and the forward path has the same period with the backward path. The generated closed curve is approximated by EFDs. Although the Fourier coefficients obtained is not essentially the Fourier coefficients for the open curve of interest, they can be used to reconstruct the open curve by using half period. As a result, the Fourier coefficients obtained for the converted curve can be written as

$$\begin{bmatrix} a_n & b_n \\ c_n & d_n \\ e_n & f_n \end{bmatrix}_{\text{cvt}} = \begin{bmatrix} \frac{4}{n^2\pi}\sum_{p=1}^{K}\frac{\Delta x_p}{\Delta L_p}\left(\cos\frac{nt_p}{2}-\cos\frac{nt_{p-1}}{2}\right) & 0 \\ \frac{4}{n^2\pi}\sum_{p=1}^{K}\frac{\Delta y_p}{\Delta L_p}\left(\cos\frac{nt_p}{2}-\cos\frac{nt_{p-1}}{2}\right) & 0 \\ \frac{4}{n^2\pi}\sum_{p=1}^{K}\frac{\Delta z_p}{\Delta L_p}\left(\cos\frac{nt_p}{2}-\cos\frac{nt_{p-1}}{2}\right) & 0 \end{bmatrix} \quad (5)$$

where the subscript "cvt" denotes the open curves of interest re-described by the converted model. The constant terms do not change since the shape center is the same. For detail derivations, the reader can refer to Chang (2024). It can be seen that each a_n has identical values for both forward and backward paths, as do coefficients c_n and e_n. Meanwhile, (b_n, d_n, f_n) remain consistently zero. It also implies that the ellipse drawn by the corresponding harmonic now degenerates into a line, as shown in Fig. 3(b).

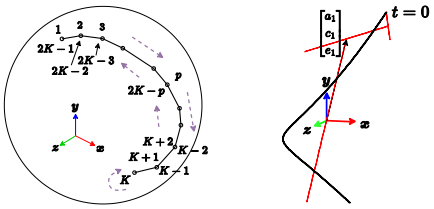

(a) (b)

Fig. 3. Convert an open curve to (a) a closed curve model, and (b) a contour described by a series of degenerated ellipses (lines).

Normalization Process

To compare the dissimilarity among various curves, it is necessary to convert the curves into a normalized form so that variances in the shape topology can be removed. These variances include position, orientation, scale, and starting point of each curve. The normalization process can be performed as follows.

1. Position. The centroid of the curve is moved to the origin of the coordinate system. This corresponds to eliminating the constant term $[A_0 \ C_0 \ E_0]^{\mathrm{T}}$ from Eq. (1).
2. Starting point. The starting point on the first ellipse is standardized by shifting it from its original place to the end of the semi-major axis $\boldsymbol{u}_1$. Such phase shift from *t*=0 to (t+ θ_1) will require a postmultiplication of the Fourier coefficients in Eq. (1) by a transformation matrix containing the phase shift angle θ_1 as

$$\begin{bmatrix} a_n & b_n \\ c_n & d_n \\ e_n & f_n \end{bmatrix}^{*} = \begin{bmatrix} a_n & b_n \\ c_n & d_n \\ e_n & f_n \end{bmatrix} \begin{bmatrix} \cos n\theta_1 & -\sin n\theta_1 \\ \sin n\theta_1 & \cos n\theta_1 \end{bmatrix} \quad (6)$$

where the matrix with superscript "*" denotes the updated state. The phase shift θ_1 can be obtained from the trigonometry of the first ellipse as

$$\theta_1 = \frac{1}{2}\tan^{-1}\frac{2(a_1b_1+c_1d_1+e_1f_1)}{a_1^2+c_1^2+e_1^2-b_1^2-d_1^2-f_1^2} \quad (7)$$

It can be noted that the starting point on the first ellipse can be classified into two types: one at the end of the semi-major axis and the other at a rotation of θ_1 radians from the previous end, ($\theta_1 + \pi$). Choosing the latter classification may represent the same curve but yield a sign change in the coefficients for the even harmonics. In this study, we choose the former expression and thus modify the coefficients as

$$\begin{bmatrix} a_n & b_n \\ c_n & d_n \\ e_n & f_n \end{bmatrix}^{*} = \zeta_n \begin{bmatrix} a_n & b_n \\ c_n & d_n \\ e_n & f_n \end{bmatrix} \begin{bmatrix} \cos n\theta_1 & -\sin n\theta_1 \\ \sin n\theta_1 & \cos n\theta_1 \end{bmatrix} \quad (8.a)$$

where

$$\zeta_n = \begin{cases} (-1)^n, \text{if } (N > 1) \text{ and } (|\boldsymbol{u}_2^* - \boldsymbol{u}_1^*| + |\boldsymbol{v}_2^* - \boldsymbol{v}_1^*| > |\boldsymbol{u}_2^* + \boldsymbol{u}_1^*| + |\boldsymbol{v}_2^* + \boldsymbol{v}_1^*|) \\ 1, \text{otherwise} \end{cases} \quad (8.b)$$

and where $\mathbf{u}_n^* = [a_n^*, c_n^*, e_n^*]^T$ and $\mathbf{v}_n^* = [b_n^*, d_n^*, e_n^*]^T$.

3. Orientation. The orientation of the curve can be standardized by aligning the semi-major and semi-minor axes with the *x*- and *y*- axes of the fixed coordinate system, respectively. We define a local coordinate system on the first ellipse whose *x*-axis is the semi-major axis and *y*-axis is the semi-minor axis. A rotation matrix R_ψ that transforms the local coordinate to the fixed coordinate can be then established as

$$R_\psi = \left[\frac{\boldsymbol{u}_1^*}{|\boldsymbol{u}_1^*|} \quad \frac{\boldsymbol{v}_1^*}{|\boldsymbol{v}_1^*|} \quad \frac{\boldsymbol{u}_1^* \times \boldsymbol{v}_1^*}{|\boldsymbol{u}_1^* \times \boldsymbol{v}_1^*|}\right] \quad (9)$$

As a result, the orientation normalization can be attained by pre-multiplying the transpose of the rotation matrix to the coefficient matrix as

$$\begin{bmatrix} a_n & b_n \\ c_n & d_n \\ e_n & f_n \end{bmatrix}^{**} = R_\psi{}^T \begin{bmatrix} a_n & b_n \\ c_n & d_n \\ e_n & f_n \end{bmatrix} \quad (10)$$

where the superscript "**" denotes the normalized coefficients. This also means to represent the coordinate of the fixed frame in terms of the coordinate system of the first ellipse. On the other hand, for the case of the open curves, as the semi-minor axis vanishes, we choose the semi-major axis of the second harmonic to replace the semi-minor axis in Eq. (9). Therefore, the rotation matrix for an open curve can be written as

$$R_{\psi,\text{open}} = \left[\frac{\boldsymbol{u}_1^*}{|\boldsymbol{u}_1^*|} \quad \frac{(\boldsymbol{u}_1^* \times \boldsymbol{u}_2^*) \times \boldsymbol{u}_1^*}{|(\boldsymbol{u}_1^* \times \boldsymbol{u}_2^*) \times \boldsymbol{u}_1^*|} \quad \frac{\boldsymbol{u}_1^* \times \boldsymbol{u}_2^*}{|\boldsymbol{u}_1^* \times \boldsymbol{u}_2^*|}\right] \quad (11)$$

Thus, one can obtain normalized Fourier coefficients in orientation for open curves by substituting Eq. (11) into Eq. (10).

4. Scale. Finally, the scale invariance can be achieved by dividing the coefficients with the semi-major axis length of the first ellipse $s = |\boldsymbol{u}_1^*| = \sqrt{a_1^{*2} + c_1^{*2}}$, where a_1^* and c_1^* are the Fourier coefficient obtained in Eq. (8.a).

From the above discussion, the normalized coefficients can be summarized as

$$\begin{bmatrix} a_n & b_n \\ c_n & d_n \\ e_n & f_n \end{bmatrix}_{\text{Norm}} = \frac{1}{s} R_\psi{}^T \left(\zeta_n \begin{bmatrix} a_n & b_n \\ c_n & d_n \\ e_n & f_n \end{bmatrix} \begin{bmatrix} \cos n\theta_1 & -\sin n\theta_1 \\ \sin n\theta_1 & \cos n\theta_1 \end{bmatrix}\right) \quad (12)$$

Minimum Harmonic Detection

The accuracy of the contour's description is typically determined by the number of harmonics used. Usually, only a few initial harmonics are necessary to precisely describe the contour. Nonetheless, in specific cases such as portions with high curvature, more harmonics might be needed to ensure an accurate result. In this work, we employ Fourier Power Analysis (FPA) to find the minimum harmonic required to achieve a certain error threshold. The FPA process is defined as follows:

$$S_n = a_n^2 + b_n^2 + c_n^2 + d_n^2 + e_n^2 + f_n^2 \quad (13.a)$$

$$\underset{N \in \mathbb{Z}^+}{\text{argmin}} \frac{\sum_{n=1}^{N} S_n}{\sum_{n=1}^{M} S_n} \geq \text{Threshold} \quad (13.b)$$

where S_n is the Fourier power spectrum of the n^{th} harmonic, and a "Threshold" 99.99% is used in this study. The initial harmonic number M follows the Nyquist frequency rule, which is the half of the point number K if the curve is sampled from a known function. Otherwise, M is set to the point number K. The final harmonic number N is determined by the first accumulated spectrum that satisfies the specified threshold. This can be achieved through the implementation of a binary search algorithm in the spectrum lookup table.

SPHERICAL FOUR-BAR LINKAGE

Linkage Parameters

Figure 4 shows a general spherical four-bar linkage located on a sphere with a sphere center at $O_s(o_{sx}, o_{sy}, o_{sz})$ and sphere radius r. Points P_1, P_2, P_3, and P_4 are the pivots locations while P_5 is the coupler point on link P_3P_4. Moreover, position of P_1 is defined by the spherical coordinate parameters (η, φ) where η is the polar angle, and φ is the azimuthal angle. l_i (i=1~5) represents the length of link i and is in radian unit. l_2 serves as the input link and l_4 as the output link. γ is an angle parameter for the coupler point on the coupler. α is the angle between the reference link (frame) P_1P_2 and z-x plane. Thus, there are a total of 13 parameters to describe the spherical four-bar linkage as (o_{sx}, o_{sy}, o_{sz}, r, l_1, l_2, l_3, l_4, l_5, η, φ, γ, α). Nonetheless, $O_s(o_{sx}, o_{sy}, o_{sz})$, $P_1(\eta, \varphi)$, and α are related to the position and orientation of the coupler curve. They can be made invariant to the shape of the curve by normalization. Radius r can also be normalized by scaling. Therefore, the design parameters can be reduced to links lengths and angle parameter for the coupler point on the coupler as (l_1, l_2, l_3, l_4, l_5, γ). Relations between the pivot positions on the sphere and the design parameters are given in Appendix.

As our focus lies in creating spherical linkages capable of producing both closed and open curves, it becomes essential to determine the motion range of

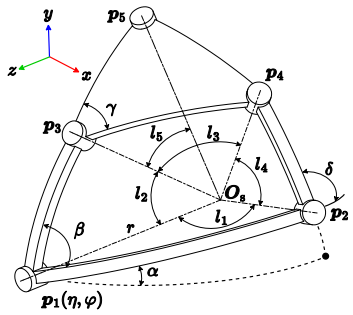

Fig. 4. Linkage parameters of a spherical four-bar linkage. The link between P_1 and P_2 is the reference link and considered the ground link in the original design, though its orientation may change after normalization.

the input link. Chiang (1984) proposed a technique to enable the classification of the driver link's range of motion for the spherical four-bar linkage, which is similar to the approach used in planar four-bar linkages. It is worth noting that placing the joint pivot on the opposite side of the sphere's surface can result in another configuration with the same range of crank motion. To prevent this, the link lengths must be adjusted so that, at most, one link length falls within the range of [π/2, π], while the lengths of the other links are less than π/2. Finally, the link lengths in radians can be treated as the planar four-bar linkage, which can be further classified by the Grashof condition and obtain the range of motion for the input link. Table 1 shows the relations between the links lengths (in radians) and types of the spherical four-bar linkages.

Table 1. Range of motion and corresponding conditions of input link.

Type	Condition	Range of Motion	Remark
Double-crank, Crank Rocker	Eq. (14.a)	[0, 2π]	Grashof, 2 circuits
Double Rocker 1	Eq. (14.b)	Eq. (15.a)	Non-Grashof, 1 circuit
Double Rocker 2	Eq. (14.c)	Eq. (15.b)	Non-Grashof, 1 circuit
Double Rocker 3, Rocker-crank	Eq. (14.d)	Eq. (15.c) or Eq. (15.d)	Grashof, 1 or 2 circuits

$$(l_1 + l_2 \le l_3 + l_4) \text{ and } (|l_1 - l_2| > |l_3 - l_4|) \quad (14.a)$$
$$(l_1 + l_2 > l_3 + l_4) \text{ and } (|l_1 - l_2| > |l_3 - l_4|) \quad (14.b)$$
$$(l_1 + l_2 < l_3 + l_4) \text{ and } (|l_1 - l_2| < |l_3 - l_4|) \quad (14.c)$$
$$(l_1 + l_2 > l_3 + l_4) \text{ and } (|l_1 - l_2| < |l_3 - l_4|) \quad (14.d)$$

$$[-\cos^{-1}\tfrac{l_1^2+l_2^2-(l_3+l_4)^2}{2l_1l_2}, \cos^{-1}\tfrac{l_1^2+l_2^2-(l_3+l_4)^2}{2l_1l_2}] \quad (15.a)$$
$$[\cos^{-1}\tfrac{l_1^2+l_2^2-(l_3-l_4)^2}{2l_1l_2}, 2\pi - \cos^{-1}\tfrac{l_1^2+l_2^2-(l_3-l_4)^2}{2l_1l_2}] \quad (15.b)$$
$$\left[\cos^{-1}\tfrac{l_1^2+l_2^2-(l_3-l_4)^2}{2l_1l_2}, \cos^{-1}\tfrac{l_1^2+l_2^2-(l_3+l_4)^2}{2l_1l_2}\right] \quad (15.c)$$
$$[2\pi - \cos^{-1}\tfrac{l_1^2+l_2^2-(l_3-l_4)^2}{2l_1l_2}, 2\pi - \cos^{-1}\tfrac{l_1^2+l_2^2-(l_3+l_4)^2}{2l_1l_2}] \quad (15.d)$$

Optimization Method

To find the curve closest to the target curve, an optimization program in this work is developed as

$$\text{Min } E = \sum_{n=1}^{N}(|\Delta a_n| + |\Delta b_n| + |\Delta c_n| + |\Delta d_n| + |\Delta e_n| + |\Delta f_n|), \quad (16)$$

Subject to

$$l_{\min} \le l_i \ (i=1\sim5) \le l_{\max}$$
$$\gamma_{\min} \le \gamma \le \gamma_{\max}$$

where the prefix "Δ" represents the difference between the normalized coefficient of target curve and that of synthesized one. $l_{\min}$ and $l_{\max}$ are the lower and upper limits of link lengths, respectively. Further, we employ the Differential Evolution (DE) algorithm (Storn and Price, 1997) to optimize the linkage parameters according to the EFD error. DE is a population-based evolutionary algorithm that is suitable for non-continuous optimization problems. The DE algorithm has three leading operators: mutation, crossover, and selection. The mutation operator introduces diversity into the population, ensuring exploration of the design space. It is defined as:

$$(\boldsymbol{x}_{\text{trial}})_s = (\boldsymbol{x}_{\text{current best}})_s + F[(\boldsymbol{x}_{r1})_s - (\boldsymbol{x}_{r2})_s] \quad (17)$$

where $\boldsymbol{x}_{r1}, \boldsymbol{x}_{r2}$ are the variables of two randomly selected individuals without repetition, s is the variable index determined by the crossover operator, and F is the mutation factor between 0 and 1, controlling the magnitude of variation. This operation directs the trial solution toward the best-performing individual while preserving population diversity. The trial offspring is closer to the current best with some random variation. The crossover operator uses a continuous selection method, where a randomly chosen index and segment length determine the variables to be replaced in the current individual, forming the trial offspring. The selection step evaluates the trial offspring using the objective function Eq. (16). If the trial offspring has a lower error than the current individual, it replaces the latter; otherwise, the original individual is retained. This process continues until either the error reaches a predefined threshold or the maximum number of iterations is met. At the start, initial individuals may have high error values, meaning poor linkage configurations. As iterations progress, mutation and crossover refine the solutions, reducing the error and guiding the population toward convergence. The final optimized linkage minimizes shape discrepancy, ensuring that the synthesized coupler curve closely follows the target path. Unless specified otherwise, our

parameters include 50 iterations, a population size of 200, a mutation factor (F) of 0.6, a cross probability of 90%, and a fixed random seed set of 0 for reproducibility.

The objective function receives the linkage parameters $(l_1, l_2, l_3, l_4, l_5, \gamma)$ as input and first filters out infeasible solutions for the cases that violate assembly constraints or the required range of motion. For feasible solutions, it generates the coupler curves for each circuit and approximate them using normalized EFDs. The error between the target and the approximated EFDs is then calculated using the L1 norm as shown in Eq. (16). Figure 5 illustrates the workflow of the objective function within the DE algorithm.

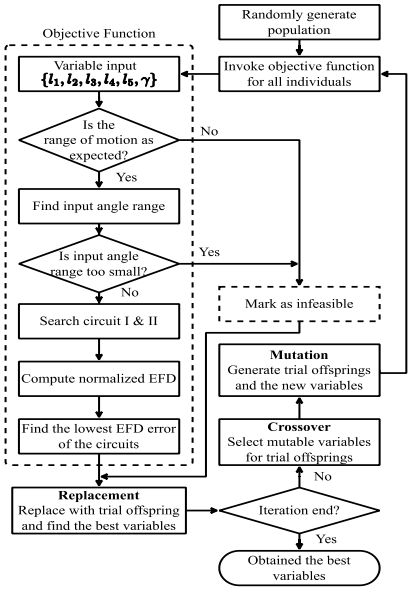

Fig. 5. Workflow of DE algorithm and the objective function.

Denormalization

Once the optimal linkage is found, the denormalization process is required to convert the normalized data back to the data in target space, including the location of the sphere center O_s, orientation, and the radius r of the sphere. This can be formulated as

$$O_{s,\text{denorm}} = \begin{bmatrix} A_0 \\ C_0 \\ E_0 \end{bmatrix}_{\text{tar}} - \begin{bmatrix} A_0 \\ C_0 \\ E_0 \end{bmatrix}_{\text{syn}} \quad (18.a)$$

$$\mathrm{R}_{\text{sphere,denorm}} = \left(\mathrm{R}_{\psi}\right)_{\text{syn}} \left(\mathrm{R}_{\psi}^{\mathrm{T}}\right)_{\text{tar}} \quad (18.b)$$

$$r_{\text{denorm}} = \frac{s_{\text{tar}}}{s_{\text{syn}}} \quad (18.c)$$

where the subscript "tar" denotes values in the target space and "syn" denotes values obtained in the normalization process. Next, the position of $\mathrm{P}_1(p_{1x}, p_{1y}, p_{1z})$ can be calculated from

$$\boldsymbol{O_s P_1} = \mathrm{R}_{\text{sphere,denorm}} r_{\text{denorm}} \hat{\boldsymbol{k}}, \quad (19)$$

Once the position of P_1 is known, the rest positions of the pivots of the spherical four-bar linkage can be calculated through the equations (A.1) to (A.13) in Appendix where $\mathrm{R}_{\text{sphere}}$, and r are replaced by $\mathrm{R}_{\text{sphere,denorm}}$ and r_{denorm}, respectively.

EXAMPLES

Example Cases and Implementations

In this section, we present five examples to show the effectiveness of the synthesis method. Throughout this study, the link lengths l_i (i=1~5) are confined within the range [0.0001, π] while γ is defined within the interval [0, π]. The calculations are implemented on a PC with Intel i5-9400F CPU, and the software is developed using the Rust programming language. The examples have three case types: closed curve matching and open curve matching, both employing a full range of motion to traverse the target curve; and the third type, which mimics a flapping-wing curve. In the linkage plot, the sphere is rendered in gray, the links in front of the sphere are rendered in black, and the links behind the sphere (hidden from the viewer) are rendered as dashed lines of darker gray.

Example 1 This example considers the coupler curve spanning more than a hemisphere as shown in Fig. 1(a) as a target. The synthesized result successfully generates the desired coupler path as shown in Fig. 6. The design parameters for the target and the optimized linkages are listed in Table 2. The optimized linkage exhibits a crank-rock behavior. Additionally, due to the path extending beyond a hemisphere, this case demonstrates the advantage of the spatial EFD approach over projection-based methods, which would introduce distortions in Fourier coefficient computation.

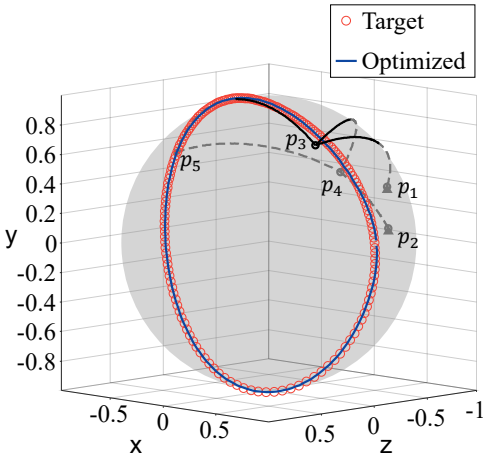

Fig. 6. Example 1 coupler curve spanning over a hemisphere

Table 2 Linkage parameters of Example 1

	o_{sx}	o_{sy}	o_{sz}	r	η	φ
Target	0	0	0	1	3.1191	0.8965
Opti-mized	-0.00	0.00	-0.00	0.999	2.783	1.024
	α	l_1	l_2	l_3	l_4	l_5
Target	0	0.488	2.353	1.083	2.053	2.462
Opti-mized	0.62	0.300	1.408	1.618	0.52	0.394
	γ	**Circuit**	**Error *E***	**Harmonic**	**Time**	
Target	2.885	II	N/A	N/A	N/A	
Opti-mized	1.946	I	0.0073	3	519 ms	

Example 2 This example consider a closed curve defined by 64 points adopted from Chu and Sun (2010). The reference study utilized an atlas-based search approach without an optimization process. In our work, a dataset of 102,400 samples was established as an atlas with uniform probability distribution, occupying a storage size of 96.8 MB. The DE algorithm, as outlined in Section 3.2, was then applied for an optimal linkage. Fig. 7 compares the results obtained from the atlas and the optimization, while Table 3 lists the linkage parameters. Additionally, Table 4 shows the normalized coefficients for the target curve, consisting of five harmonics and a total of 30 coefficients. The comparison highlights the advantages of combining atlas-based methods with evolutionary optimization. While the atlas method provides an initial approximation, DE fine-tunes the linkage configuration, reducing synthesis error and improving the fidelity of the generated curve.

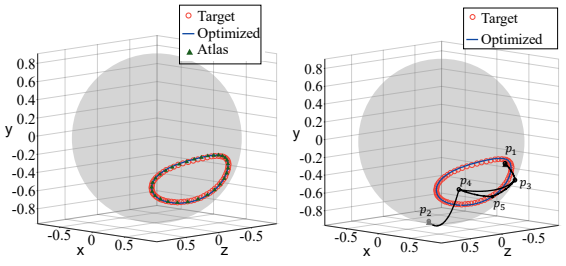

Fig. 7. Example 2 (a) Curve comparison (b) Schematic of synthesized linkage.

Table 3. Linkage parameters of Example 2.

	o_{sx}	o_{sy}	o_{sz}	r	η	φ
EFD Atlas	0.01	0.00	0.00	0.98	0.93	-0.99
Optimized	0.06	-0.02	0.01	0.93	1.65	-0.16
	α	l_1	l_2	l_3	l_4	l_5
EFD Atlas	-1.94	1.17	2.69	2.02	1.23	1.97
Optimized	-1.72	1.62	0.49	0.96	1.30	1.46
	γ	Circuit	Error E	Harmonic	Time	
EFD Atlas	2.61	II	0.0647	5	N/A	
Optimized	0.43	II	0.0522	5	292.45 ms	

Table 4. Normalized EFD coefficients of the target curve of Example 2.

Harmonic No.	*a*	*b*	*c*	*d*	*e*	*f*
1	1	0	0	0.6439	0	0
2	0.0001	-0.0007	-0.0020	-0.0001	-0.0901	0.0003
3	0.0558	0.0022	0.0062	0.0519	-0.0001	0.0006
4	-0.0002	-0.0004	0.0008	0.0008	-0.0099	-0.0022
5	0.0092	0.0023	-0.0010	0.0092	0.0002	0

Example 3 This example considers the analemma, the apparent path of the sun in the sky relative to an Earth observer, forming an asymmetrical figure-eight on a unit spherical surface. This trajectory, relevant to solar tracking mechanisms, is computed using equations (6)–(8) from Zhang et al. (2021) and the sunpos subroutine:

$$P_T = \text{sunpos}(T_{\text{GMT}}, \text{longitude}, \text{latitude})$$

where T_{GMT} represents the date and time in GMT form and expressed as a float number. In this analysis, 100 points were extracted from December 4, 2023 at 8:00 am to December 4, 2024 at 8:00 am., with (longitude, latitude) specified by (60.960515°, 23.69781°). All other constants in the subroutine remain consistent. The resulting curve is illustrated in Fig. 8, and the corresponding synthesized linkage parameters are presented in Table 5. The optimized spherical four-bar linkage successfully generates the figure-eight trajectory, demonstrating the applicability of the proposed method to celestial tracking problems. The synthesized path closely follows the target curve, with minimal deviation. This example further underscores the capability of the spatial EFD approach in accurately modeling real-world, non-uniform spherical trajectories.

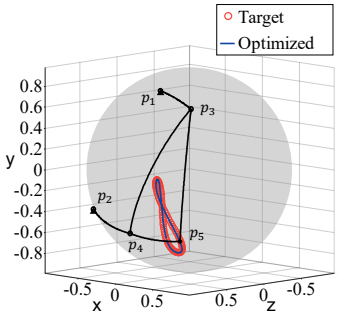

Fig. 8. Linkage synthesis of Example 3.

Table 5. Linkage parameters of Example 3.

	o_{sx}	o_{sy}	o_{sz}	r	η	φ
Optimized	0.00	0.00	0.01	0.98	1.02	1.41
	α	l_1	l_2	l_3	l_4	l_5
Optimized	-2.21	1.53	0.41	1.48	0.62	1.06
	γ	Circuit	Error E	Harmonic	Time	

Optimized	1.36	I	0.0563	10	362.81 ms	

Example 4 This example considers an open curve similar to Example 2 in Sun et al. (2018) but with a different parametric formulation. Unlike Sun et al. (2018), which employed a Wavelet Transform (WT) approach, our method utilizes spatial EFDs to synthesize the mechanism. The curve is defined by the parametric formula:

$$\begin{cases} x(\theta) = \sin 65° \sin(-0.4685°\theta + 173.1994°) \\ y(\theta) = -\cos\theta \cos(-0.4685°\theta + 173.1994°) \\ \quad + \cos 65° \sin\theta \sin(-0.4685°\theta + 173.1994°) \\ z(\theta) = -\sin\theta \cos(-0.4685°\theta + 173.1994°) \\ \quad - \cos 65° \cos\theta \sin(-0.4685°\theta + 173.1994°) \end{cases}$$

where the angle argument θ ranges from 40° to 320°, and 40 points are collected as input. The synthesized result successfully reconstructs the target trajectory, as shown in Fig. 9, with the optimized linkage parameters presented in Table 6. The mechanism operates as a double-rock, ensuring smooth movement within the specified input range. The optimization results indicate that increasing the number of harmonics and iterations enhances accuracy, with only a limited increase in computation time (up to 1.22 seconds).

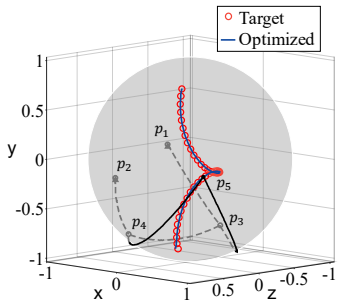

Fig. 9. Synthesized linkage of Example 4

Table 6. Linkage parameters of Example 4.

	o_{sx}	o_{sy}	o_{sz}	r	η	φ
Optimized	0.00	0.00	-0.06	1.03	2.13	-3.13
	α	l_1	l_2	l_3	l_4	l_5
Optimized	-0.44	0.68	1.00	0.99	0.65	2.55
	γ	Circuit-Branch	Error E	Harmonic	Time	
Optimized	3.14	II-I	0.0633	19	1.458 s	

Example 5 This example is inspired by McDonald and Agrawal (2010) where a spherical four-bar linkage was explored for flapping-wing motion. The reference initially used a 3-DOF serial chain with angle parameters ϕ, ψ, and θ, defined through a Denavit-Hartenberg transformation matrix. In our work, we use the following parametric equations to generate our target motion:

$$\phi = 0.6\sin(\omega t) + 0.5$$
$$\psi = 0.8\cos(\omega t) - 0.3$$
$$\theta = 0.25\cos(\omega t) + 0.25$$

where the input angle ωt varies within $[0, 2\pi]$. The target curve is generated by a point on the end effector as $[-0.06, 0.01, 0, 1]^T$, and its position in the reference frame is given by:

$$P = \mathrm{T}_{\mathrm{DH}} \begin{bmatrix} -0.06 \\ 0.01 \\ 0 \\ 1 \end{bmatrix},$$

where the D-H transformation matrix is

$$\mathrm{T}_{\mathrm{DH}} = \begin{bmatrix} \sin\phi\sin\theta + \cos\sigma\cos\phi\cos\theta & \sin\sigma\cos\phi & \cos\sigma\cos\phi\sin\theta - \cos\theta\sin\phi & 0.015\sin\phi \\ \cos\sigma\cos\theta\sin\phi - \cos\phi\sin\theta & \sin\sigma\sin\phi & \cos\phi\cos\theta + \cos\sigma\sin\phi\sin\theta & -0.015\cos\phi \\ \sin\sigma\cos\theta & -\cos\sigma & \sin\sigma\sin\theta & 0 \\ 0 & 0 & 0 & 1 \end{bmatrix}$$

and $\sigma = (\psi - \pi/2)$. Since the target shape is not a spherical curve, the optimized curve serves as an approximate curve that closely mimics the intended shape. Figure 11 illustrates the comparison between the target and synthesized curves, while Fig. 12 depicts the synthesized spherical four-bar linkage. The final linkage parameters are listed in Table 9. The optimized linkage effectively replicates the flapping trajectory, ensuring smooth continuous motion across the defined input range. The synthesis demonstrates the capability of spatial EFDs in approximating non-spherical trajectories, providing an efficient alternative to serial-chain mechanisms for flapping-wing applications.

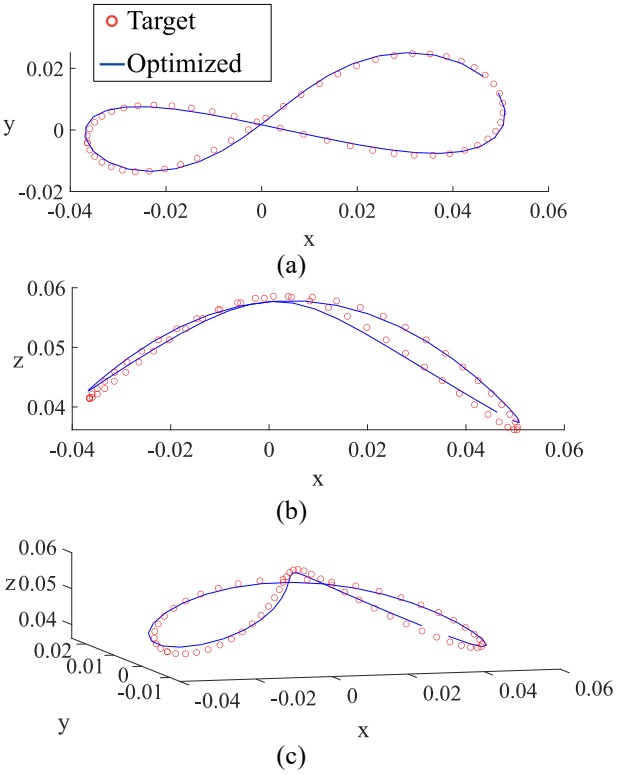

Fig. 10. Curve comparison of Example 6 in (a) x-y plane, (b) x-z plane, and (c) perspective view.

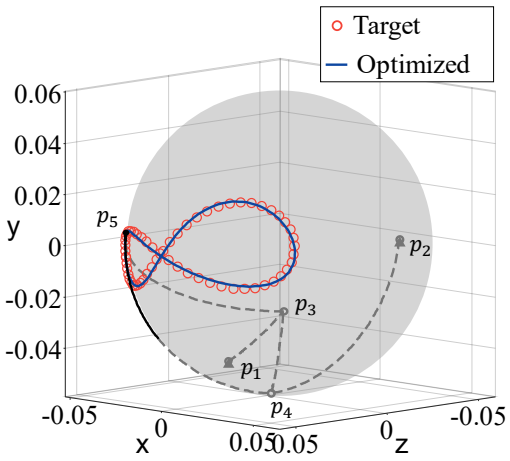

Fig. 11. Schematic of synthesized linkage of Example 5.

Table 7. Linkage parameters of Example 6.

	o_{sx}	o_{sy}	o_{sz}	r	η	φ
Optimized	0.00	0.00	0.00	0.05	1.64	-2.14
	α	l_1	l_2	l_3	l_4	l_5
Optimized	-2.02	1.49	0.59	0.86	1.48	0.16
	γ	Circuit	Error E	Harmonic	Time	
Optimized	2.68	1	0.0877	6	421.49 ms	

Discussions

1. Handling of Curves Spanning More than a Hemisphere

Figure 1 illustrates a case where the curve extends beyond a hemisphere, posing challenges for traditional Fourier Descriptors (FDs), which often rely on projection-based methods that introduce distortions. In contrast, Elliptical Fourier Descriptors (EFDs) independently analyze each component in 3D space, preserving geometric integrity and achieving superior approximation accuracy.

2. Choice of EFDs over Other Shape Representation Methods

EFDs offer a practical and efficient alternative to complex shape representation techniques like wavelet transforms (WT) (Sun et al., 2015, 2018). While WT handles both closed and open curves well, it requires careful function selection and multi-level decomposition, increasing computational cost. EFDs, in contrast, efficiently decompose curves into harmonic components, making them easier to apply in spherical mechanism design.

3. Open Curve Approximation: Accuracy vs. Computation

Example 4 highlights the trade-off between accuracy and computational cost. Slight mismatches occur at the open curve's lower end, with higher harmonics increasing search time. Fourier Power analysis helps balance this by selecting the minimum necessary harmonics to maintain accuracy while keeping computation time low.

Table 8 Comparison of the Proposed Method with Existing Approaches

Aspect	Previous Work	Current Work (Spatial EFD + DE)	Contribution
Path Representation	Planar FDs for 2D(McGarva, 1994) linkages or projection-based FDs, WT (Sun, 2018) for spherical linkages	Spatial EFDs	Systematic extension of EFDs to spherical four-bar linkage synthesis
Optimization Method	Atlas-based search(Chu& Sun, 2010), Simulated annealing for 2D	Differential Evolution (DE)	-
Handling of Open Curves	Requires ad hoc modifications	Direct shape signature approach using EFDs	New unified approach for both open and closed curves
Computation Efficiency	Not available	Less than 1.22 sec. in open path example	-

4. Effectiveness and Limitations of DE Optimization

DE is highly effective for optimizing spherical linkage design with 6 to 8 parameters, offering a robust search strategy for multimodal solution spaces. While it does not guarantee a global optimum, mutation, crossover, and selection help prevent local minima. For higher precision, future work could explore multiple DE runs with varying initial populations or hybridizing with other optimization techniques.

5. Table 8 highlights the key differences between previous approaches and the current study.

CONCLUSIONS

In this study, we developed a unified methodology for the path synthesis of spherical four-bar linkages, enabling the synthesis of both closed and open curves using a single framework. Unlike previous approaches that required separate treatments or modifications for different curve types, our method systematically extends Elliptical Fourier Descriptors (EFDs) to 3D space, eliminating the need for planar projections and preserving geometric integrity.

We demonstrated the effectiveness of the proposed method through a range of examples, including an ordinary closed curve, a figure-8 shape curve, an open curve, and real-world applications as solar tracking (analemma) and flapping-wing motion. The unified algorithm also exhibits computationally efficient, solving most examples in less than 500 ms, and handling complex scenarios as Example 4 in just 1.22 seconds. We anticipate its broader applicability in advanced spatial mechanism design.

NOMENCLATURE

A_0, C_0, E_0 EFD constant terms

$a_n, b_n, c_n, d_n, e_n, f_n$ EFD coefficients of the nth harmonic
E EFD error
F Mutation factor in differential evolution algorithm
K Total number of given points on a curve
l_1, l_2, l_3, l_4, l_5 Link length variables in radians
$l_{\min}, l_{\max}$ Lower and upper limits of links in the optimization
M Initial harmonic number in FPA
n Harmonic number
N Total harmonic number
P_1, P_2, P_3, P_4, P_5 Points on the spherical linkage
r Radius of sphere
s Scale factor
S_n The nth Fourier power spectrum
t Time parameter
$\boldsymbol{u}_1, \boldsymbol{v}_1$ First semi-major and semi-minor axes
$\boldsymbol{x}$ Design variable vector in the optimization
$x(t), y(t), z(t)$ Curve components with time parameter t
α Rotation angle of the ground link
γ Angle of coupler point P_5 on the coupler link
$\Delta x_p, \Delta y_p, \Delta z_p, \Delta L_p$ Distance between P and $P+1$ point along each component x, y, z, and the magnitude
ζ_n Correction factor of the nth harmonic in the normalization
η, φ Polar and azimuthal angles of point P_1 to the sphere
θ_1, θ_n Phase angle of the first and the nth harmonic in the normalization
ψ, R_ψ Rotation angle of the shape and its rotation matrix in the normalization

REFERENCE

Arata J, Kobayashi Y, Nakadate R, Onogi S, Kiguchi K, & Hashizume M. "Spherical and Non-Spherical Combined Two Degree-of-Freedom Rotational Parallel Mechanism for a Microsurgical Robotic System," J. Robotics Mechatronics, 30, 846-854 (2018).

Bagci C. "Geometric methods for the synthesis of spherical mechanisms for the generation of functions, paths and rigid-body positions using conformal projections." Mechanism and Machine Theory 19:113–127 (1984).

Caple J, Byrd J, Stephan CN. "Elliptical Fourier analysis: fundamentals, applications, and value for forensic anthropology." Int J Legal Med 131:1675–1690 (2017).

Chablat D, Angeles J. "The computation of all 4R serial spherical wrists with an isotropic architecture." ASME Journal of Mechanical Design 125:275-280 (2003).

Chang Y. "Kinematic Synthesis of Planar and Spherical Four-Bar Linkages Using Elliptical Fourier Descriptors" Doctoral dissertation, Department of Mechanical Engineering, National Taiwan University, Taipei, Taiwan (2024).

Chang Y, Chang JL & Lee JJ. "Path synthesis of planar four-bar linkages for closed and open curves using elliptical Fourier descriptors." J Mech Sci Technol 38, 2579–2590 (2024).

Chiang CH. "On the classification of spherical four-bar linkages." Mechanism and Machine Theory 19:283–287 (1984).

Chiang CH. Kinematics of Spherical Mechanism. McGraw-Hill Int'l Enterprises Inc, Taiwan (1986).

Chu J, Sun J. "Numerical atlas method for path generation of spherical four-bar mechanism." Mechanism and Machine Theory 45:867–879 (2010).

Crampton JS. "Elliptic Fourier shape analysis of fossil bivalves: some practical considerations." LET 28:179–186 (1995).

Galán-Marín G, Alonso FJ, Del Castillo JM. "Shape optimization for path synthesis of crank-rocker mechanisms using a wavelet-based neural network." Mechanism and Machine Theory 44:1132–1143 (2009).

Godefroy JE, Bornert F, Gros CI, Constantinesco A. "Elliptical Fourier descriptors for contours in three dimensions: A new tool for morphometrical analysis in biology." Comptes Rendus Biologies 335:205–213 (2012).

Kuhl FP, Giardina CR. "Elliptic Fourier features of a closed contour." Computer Graphics and Image Processing 18:236–258 (1982).

Lee W-T, Russell K, Shen Q, Sodhi RS. "On adjustable spherical four-bar motion generation for expanded prescribed positions." Mechanism and Machine Theory 44:247–254 (2009).

Lestrel PE Ed. Fourier Descriptors and Their Applications in Biology. Cambridge University Press, New York (1997).

Lestrel PE, and Roche A.F. "Cranial Base Shape Variation with Age: A Longitudinal Study of Shape Using Fourier Analysis." Human Biology, 58(4), 527–540 (1986).

Lin CC. "Complete Solution of the Five-Position Synthesis for Spherical Four-Bar Mechanisms." Journal of Marine Science and Technology 6:12–27 (1998).

Lin C-S, Hwang C-L. "New forms of shape invariants from elliptic Fourier descriptors." Pattern Recognition 20:535–545 (1987).

Lum MJH, Rosen J, Sinanan MN, Hannaford B. "Optimization of a spherical mechanism for a minimally invasive surgical robot: Theoretical and Experimental Approaches." IEEE Trans Biomed Eng 53:1440–1445 (2006).

McDonald M, Agrawal SK. "Design of a bio-inspired

spherical four-bar mechanism for flapping-wing micro air-vehicle applications." ASME Journal of Mechanisms and Robotics 2:021012 (2010).
McGarva JR. "Rapid search and selection of path generating mechanisms from a library." Mechanism and Machine Theory pp 223–235 (1994).
McGarva J, Mullineux G. "Harmonic representation of closed curves." Applied Mathematical Modelling 17:213–218 (1993).
Mullineux G. "Atlas of spherical four-bar mechanisms." Mechanism and Machine Theory 46:1811–1823 (2011).
Niño-Sandoval TC, Morantes Ariza CF, Infante-Contreras C, Vasconcelos BC "Evaluation of natural mandibular shape asymmetry: an approach by using elliptical Fourier analysis." Dentomaxillofacial Radiology 47:20170345 (2018).
Storn R, Price K. "Differential Evolution - a Simple and Efficient Heuristic for Global Optimization over Continuous Spaces," Journal of Global Optimization, 11(4), 341-359 (1997).
Suixian Y, Hong Y, Tian GY "Optimal selection of precision points for function synthesis of spherical 4R linkage." Proceedings of the Institution of Mechanical Engineers, Part C: Journal of Mechanical Engineering Science 223:2183–2189 (2009).
Sun J, Chu J. "Fourier series representation of the coupler curves of spatial linkages." Applied Mathematical Modelling 34:1396–1403 (2010).
Sun J, Liu W, Chu J. "Dimensional synthesis of open path generator of four-bar mechanisms using the haar wavelet." ASME Journal of Mechanical Design 137:082303 (2015).
Sun J, Liu W, Chu J. "Synthesis of spherical four-bar linkage for open path generation using wavelet feature parameters." Mechanism and Machine Theory 128:33–46 (2018).
Tsai LW. Robot Analysis: The Mechanics of Serial and Parallel Manipulators. John Wiley & Sons, New York (1999).
Ullah I, Kota S. "Optimal synthesis of mechanisms for path generation using Fourier descriptors and global search methods." ASME Journal of Mechanical Design 119:504–510 (1997).
Wang M, Leal-Naranjo J.A, Ceccarelli M and Blackmore S. "A Novel Two-Degree-of-Freedom Gimbal for Dynamic Laser Weeding: Design, Analysis, and Experimentation," in IEEE/ASME Transactions on Mechatronics, 27(6), pp. 5016-5026 (2022).
Wu J, Ge QJ, Gao F, Guo WZ. "On the extension of a Fourier descriptor based method for planar four-bar linkage synthesis for generation of open and closed paths." ASME Journal of Mechanisms and Robotics 3(3): 031002 (2011).
Zhang T, Stackhouse PW, Macpherson B, Mikovitz JC. "A solar azimuth formula that renders circumstantial treatment unnecessary without compromising mathematical rigor: Mathematical setup, application and extension of a formula based on the subsolar point and atan2 function." Renewable Energy 172:1333–1340 (2021).

ACKNOWLEDGMENT

The authors thank the support from the National Science and Technology Council, Taiwan (NSTC 112-2221-E-002-220)

Appendix Coupler Point Calculation of Spherical Four-bar Linkages

Shown in Fig. A1 is the spherical four-bar linkage whose sphere center is now located in the origin of the reference frame. The relationship between the input angle β and the output angle δ of the follower link is (Chiang, 1986)

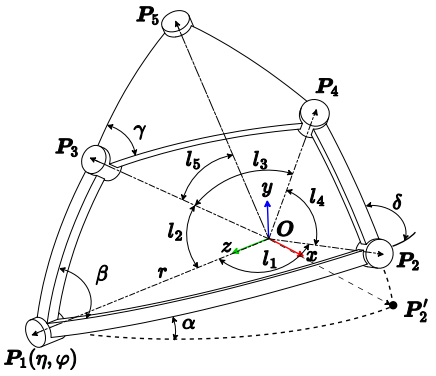

Fig. A1. Linkage parameters of a spherical four-bar linkage. Link P_1P_2 is the reference link (frame).

$$\delta = 2\tan^{-1}\frac{-h_3 \pm \sqrt{h_3^2 - h_1^2 + h_2^2}}{h_1 - h_2} \quad \text{(A.1)}$$

where

$$h_1 = \cos l_2 \cos l_4 \cos l_1 - \cos l_3 + \mathrm{z}\sin l_2 \cos l_4 \sin l_1 \cos\beta \quad \text{(A.2)}$$

$$\mathrm{h_2} = -\cos \mathrm{l_2} \sin \mathrm{l_4} \sin \mathrm{l_1} + \sin \mathrm{l_2} \sin \mathrm{l_4} \cos \mathrm{l_1} \cos \beta \quad \text{(A.3)}$$

$$h_3 = \sin l_2 \sin l_4 \sin\beta \quad \text{(A.4)}$$

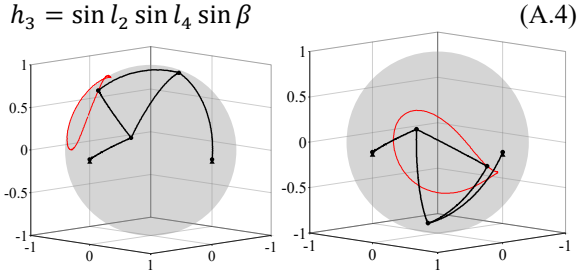

(a) (b)

Fig. A2. Two configurations, (a) circuit I and (b) circuit II, of a spherical four-bar linkage.

There are two solutions for Eq. (A.1), each equivalent to one circuit of the spherical linkages as shown in Fig. A2. We employ the screw-axis representation (Tsai, 1999) to compute the vector rotation in the spherical coordinate. Given a unit screw axis, $\boldsymbol{e}=[\boldsymbol{e_x}, \boldsymbol{e_y}, \boldsymbol{e_z}]^{\mathrm{T}}$, and angle of rotation ϕ, a rotation matrix $\mathrm{R}_{\langle \boldsymbol{e},\phi\rangle}$ that rotates a vector about the screw axis in space can be written as

$$\mathrm{R}_{\langle \boldsymbol{e},\phi\rangle} = \begin{bmatrix} \boldsymbol{e}_x^2\mu_\phi + \cos\phi & \boldsymbol{e}_x\boldsymbol{e}_y\mu_\phi - \boldsymbol{e}_z\sin\phi & \boldsymbol{e}_x\boldsymbol{e}_z\mu_\phi + \boldsymbol{e}_y\sin\phi \\ \boldsymbol{e}_x\boldsymbol{e}_y\mu_\phi + \boldsymbol{e}_z\sin\phi & \boldsymbol{e}_y^2\mu_\phi + \cos\phi & \boldsymbol{e}_y\boldsymbol{e}_z\mu_\phi - \boldsymbol{e}_x\sin\phi \\ \boldsymbol{e}_x\boldsymbol{e}_z\mu_\phi - \boldsymbol{e}_y\sin\phi & \boldsymbol{e}_y\boldsymbol{e}_z\mu_\phi + \boldsymbol{e}_x\sin\phi & \boldsymbol{e}_z^2\mu_\phi + \cos\phi \end{bmatrix} \tag{A.5}$$

where $\mu_\phi = (1-\cos\phi)$. Therefore, when rotating a vector $\boldsymbol{a}$ to another vector $\boldsymbol{b}$ about the axis ($\boldsymbol{a}\times\boldsymbol{b}$), the rotation matrix, abbreviated as ${}^{\boldsymbol{b}}\mathrm{R}_{\boldsymbol{a}}$, can be written as

$${}^{\boldsymbol{b}}\mathrm{R}_{\boldsymbol{a}} = \mathrm{R}_{\langle \frac{\boldsymbol{a}\times\boldsymbol{b}}{|\boldsymbol{a}\times\boldsymbol{b}|}, \cos^{-1}\frac{\boldsymbol{a}\cdot\boldsymbol{b}}{|\boldsymbol{a}\times\boldsymbol{b}|}\rangle}. \tag{A.6}$$

Pivot point P_1, defined by the spherical coordinates (η, φ) with sphere radius r, is transformed to the Cartesian coordinate as

$$\boldsymbol{OP_1} = \begin{bmatrix} r\sin\eta\cos\varphi \\ r\sin\eta\sin\varphi \\ r\cos\eta \end{bmatrix} \tag{A.7}$$

Positions of pivot points are computed as:

$$\boldsymbol{OP_2} = \mathrm{R}_{\mathrm{sphere}}\mathrm{R}_{\langle \hat{\boldsymbol{j}}, l_1\rangle}\cdot r\hat{\boldsymbol{k}} \tag{A.8}$$

$$\boldsymbol{OP_3} = \mathrm{R}_{\mathrm{sphere}}\mathrm{R}_{\langle \hat{\boldsymbol{k}}, \beta\rangle}\mathrm{R}_{\langle \hat{\boldsymbol{j}}, l_2\rangle}\cdot r\hat{\boldsymbol{k}} \tag{A.9}$$

$$\boldsymbol{OP_4} = \mathrm{R}_{\langle \frac{\boldsymbol{OP_2}}{|\boldsymbol{OP_2}|}, \delta\rangle}\mathrm{R}_{\langle \hat{\boldsymbol{j}}, l_4\rangle}\boldsymbol{OP_2}\ , \tag{A.10}$$

$$\boldsymbol{OP_5} = \mathrm{R}_{\mathrm{coupler}}\mathrm{R}_{\langle \hat{\boldsymbol{k}}, \gamma\rangle}\mathrm{R}_{\langle \hat{\boldsymbol{j}}, l_5\rangle}\cdot r\hat{\boldsymbol{k}} \tag{A.11}$$

where $\hat{\boldsymbol{j}}$ and $\hat{\boldsymbol{k}}$ are respectively the unit vectors of y and z axes of the coordinate, and

$$\mathrm{R}_{\mathrm{coupler}} = \begin{bmatrix} \frac{\boldsymbol{OP_3}}{|\boldsymbol{OP_3}|} & \frac{(\boldsymbol{OP_3}\times\boldsymbol{OP_4})\times\boldsymbol{OP_3}}{|(\boldsymbol{OP_3}\times\boldsymbol{OP_4})\times\boldsymbol{OP_3}|} & \frac{\boldsymbol{OP_3}\times\boldsymbol{OP_4}}{|\boldsymbol{OP_3}\times\boldsymbol{OP_4}|} \end{bmatrix} \tag{A.12}$$

$$\mathrm{R}_{\mathrm{sphere}} = \mathrm{R}_{\langle \frac{\boldsymbol{OP_1}}{|\boldsymbol{OP_1}|}, \alpha\rangle}{}^{\boldsymbol{OP_1}}\mathrm{R}_{\hat{\boldsymbol{k}}} \tag{A.13}$$